Advances in Engineering Innovation Vol.17 Issue 9 EWA Publishing
Available Online: 25 August 2026 DOI: 10.54254/2977-3903/2026.36341

Effect of base perforations on natural convection heat dissipation of a finned heat sink

Shijie Guo, Lihong Yang*

School of Mechanical Engineering, University of Shanghai for Science and Technology, Shanghai, China

*Corresponding Author. Email: lhyang@usst.edu.cn

Abstract. Conventional finned heat sinks for highly integrated electronics suffer from blocked airflow, extensive flow dead zones at fin roots and high thermal resistance under natural convection cooling. To simultaneously improve heat dissipation and reduce heat sink weight, this study proposes machining through holes on the heat sink base. Steady laminar finite volume numerical simulations are carried out to compare three perforation shapes: cylindrical, positive frustoconical and inverted frustoconical holes. We analyze how the distance between perforations and heat source influences thermal resistance and flow field, and clarify the heat transfer enhancement mechanism induced by the chimney effect of through holes. Numerical data show that cylindrical-hole heat sinks achieve a 17.44% lower thermal resistance and 15.79% lighter mass, alongside a 43.59% higher mass-specific heat transfer coefficient, compared with non-porous heat sinks. Cylindrical holes maintain uniform and stable airflow and outperform two frustoconical structures. Thermal resistance reaches the minimum value of 13.76 K/W when holes are placed close to the heat source. Base perforations form vertical air passages to suppress recirculation zones at fin roots, providing theoretical guidance for designing natural convection heat sink of high-heat-flux electronic components.

Keywords: finned heat sink, natural convection, thermal resistance, base perforations

1. Introduction

With the rapid advancement of modern electronic devices toward miniaturization, integration and high performance, the heat flux density of electronic components continues to rise. Thermal management of electronic components is critical to device performance, which has driven researchers to develop natural convection heat sinks featuring high efficiency, simple structure, reliable operation and low long-term cost for electronic cooling. However, conventional finned heat sinks share common drawbacks, including restricted airflow in fin gaps, prominent flow dead zones at fin roots and high overall thermal resistance. Accordingly, enhancing natural convection heat dissipation without significantly increasing volume and mass has become a major research focus [1].

Existing optimization strategies for heat sinks are mainly divided into two categories. The first is to optimize fin cross-sectional geometries, such as wavy and branched configurations, which improve cooling capacity by enlarging the heat transfer area or guiding near-wall flow. The second is to introduce perforation designs on fins, which ameliorate heat transfer performance by weakening flow dead zones and intensifying gas flow disturbance.

Abbas et al. [2] redesigned the fin displacement pattern to enhance natural convection heat dissipation without increasing the volume; the novel displaced fin heat sink achieved a 30% increase in heat transfer rate, a 28.7% reduction in total mass and a 27.4% decrease in surface area. Wavy fins are among the most advantageous fin types owing to their larger heat transfer area. El Ghandouri et al. [3] developed a novel rippling fin shape that reduced the thermal resistance of the radiator by 9.81%. Altun et al. [4] investigated the thermal performance of sinusoidal wavy fins with different amplitudes, and all specimens exhibited better heat transfer performance than the baseline rectangular fins, with the amplitude of H/30 delivering the optimal heat transfer effect. Chu et al. [5] introduced triangular fin protrusions at the rear of the heat sink, reducing thermal resistance by 5.5% to 7.2%. Hussain et al. [6] found that fins with rounded-edge configurations yielded better temperature uniformity and lower overall thermal resistance. Nilpueng et al. [7] explored the effects of different fin cross-sectional shapes; the results showed that under the same fin area, square cross-sectional pin fins had 12.52% higher heat transfer coefficient and 15.05% higher pressure drop than circular ones. Moayedi et al. [8] conducted systematic coupled optimization of fin number, height and bending angle, and found that increasing fin number and height and adopting straight fins could reduce thermal resistance. Zhang et al. [9] proposed W-shaped fin arrays; despite the reduced heat dissipation area, they improved cooling performance by optimizing parameters such as fin spacing and inclination angle and leveraging the flow field synergy effect.

Introducing perforations on fins is widely adopted to weaken flow dead zones and enhance local heat transfer. Karlapalem et al. [10] investigated the performance of branched fins with circular perforations under laminar natural convection, and found that although perforations reduced the surface area, they enhanced heat transfer by intensifying fluid disturbance. Sultan et al. [11] optimized fins with perforations, notches and inclined structures, which increased the average heat transfer coefficient and average Nusselt number by up to 26%. Awasarmol et al. [12] studied fin perforation designs and experimentally quantified the natural convection heat transfer performance under varying perforation diameters, configurations and inclination angles of fin arrays. Li et al. [13] explored the effects of different perforation cross-sectional shapes on three-dimensional laterally perforated finned heat sinks, established high-precision models for heat transfer enhancement ratio, friction factor reduction ratio and mass reduction ratio, and carried out multi-objective optimization, identifying square perforations as the optimal condition. Awasarmol et al. [14] confirmed that perforated fins outperform solid fins. With 12 mm-diameter perforations, the heat transfer coefficient increased by 32% and the mass decreased by 30%. They also noted that perforated fins feature lower flow resistance and superior heat transfer performance, and that increasing the number of perforations can further improve efficiency.

As demonstrated above, fin geometry optimization and perforation design have been proven effective approaches for heat dissipation enhancement. Most existing perforation schemes focus on the fin bodies, improving flow and heat transfer on fin surfaces via local perforation or cutting. To address this gap, this paper takes finned heat sinks as the research object and proposes a scheme of perforating the heat sink base. Numerical simulations are performed to investigate the effects of perforation shape and position on thermal resistance, temperature field and flow field, reveal the chimney effect and dead zone suppression mechanism of vertical through holes, and identify the optimal combination of hole shape and position. The ultimate goal is to achieve the synergy of heat transfer enhancement and structural lightweighting, and provide theoretical and data support for the engineering optimization of natural convection heat sinks for electronic components.

2. Physical model

As shown in Figure 1, the heat dissipation path of a conventional finned heat sink is as follows: heat generated by electronic components on a Printed Circuit Board (PCB) is first transferred to the heat sink base via conduction through the contact interface, then conducted from the base to the fins, and ultimately dissipated into the ambient environment through natural convection between the fins and surrounding air. This work proposes an improved design of machining through holes in the heat sink base, which optimizes the convective heat transfer conditions of the heat sink by introducing airflow from the gap between the heat sink and the PCB.

As shown in Figure 2, the research subject is a horizontally mounted rectangular finned heat sink. The geometry is symmetric with respect to both the X-Z and Y-Z central planes, and the fins are arranged in an equally spaced array. As listed in Table 1, four holes are machined in each fin gap, and the key geometric parameters are summarized. The bottom heat source, measuring 2 mm × 2 mm × 1 mm, is positioned at the exact center of the bottom surface.

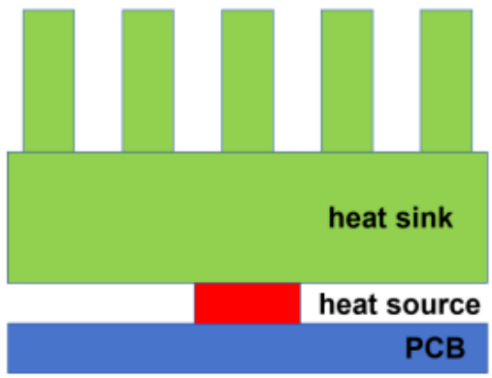

Figure 1. Schematic diagram of heat sink installation

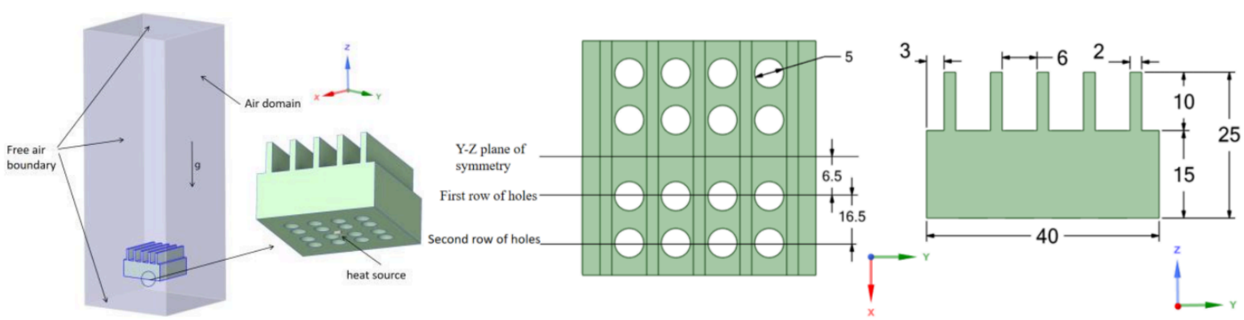

Figure 2. Schematic diagram of the heat sink

Table 1. Geometric parameters of the heat sink

Parameters	Value
Base side length L/mm	40
Total height H/mm	25
Base height H_b/mm	15
Fin height H_f/mm	10

Table 1. Continued

Fin edge distance t_s/mm	3
Fin spacing t_m/mm	6
Fin thickness t_f/mm	2
Equivalent diameter D/mm	5
Distance from the first row of holes to Y-Z plane of symmetry a/mm	6.5
Distance from the second row of holes to Y-Z plane of symmetry b/mm	14.5

3. Numerical model

Steady-state simulations are conducted. The governing equations for the fluid domain consist of the continuity equation, momentum equations and energy equation.

Continuity equation:

$$\nabla \cdot U = 0 \tag{1}$$

where U is the velocity vector in m/s, and ∇ denotes the Nabla differential operator.

Momentum equations:

$$\rho\left(u\frac{\partial u}{\partial x}+v\frac{\partial u}{\partial y}+w\frac{\partial u}{\partial z}\right)=-\frac{\partial p}{\partial x}+\mu\left(\frac{\partial^2 u}{\partial x^2}+\frac{\partial^2 u}{\partial y^2}+\frac{\partial^2 u}{\partial z^2}\right) \tag{2}$$

$$\rho\left(u\frac{\partial v}{\partial x}+v\frac{\partial v}{\partial y}+w\frac{\partial v}{\partial z}\right)=-\frac{\partial p}{\partial y}+\mu\left(\frac{\partial^2 v}{\partial x^2}+\frac{\partial^2 v}{\partial y^2}+\frac{\partial^2 v}{\partial z^2}\right) \tag{3}$$

$$\rho\left(u\frac{\partial w}{\partial x}+v\frac{\partial w}{\partial y}+w\frac{\partial w}{\partial z}\right)=-\frac{\partial p}{\partial z}+\mu\left(\frac{\partial^2 w}{\partial x^2}+\frac{\partial^2 w}{\partial y^2}+\frac{\partial^2 w}{\partial z^2}\right)-\rho g \tag{4}$$

where ρ is the air density in kg/m³; u, v, and w are the components of the velocity vector in the x, y and z directions, respectively, in m/s; μ is the dynamic viscosity of air in kg/(m·s).

Energy equation：

$$\rho c_p\left(u\frac{\partial T_a}{\partial x}+v\frac{\partial T_a}{\partial y}+w\frac{\partial T_a}{\partial z}\right)=\nabla\cdot\left(k_f\nabla T_a\right) \tag{5}$$

where c_p is the specific heat capacity of air at constant pressure in J/(kg·K); T_a is the air temperature in K; k_f is the thermal conductivity of air in W/(m·K).

The air density is modeled using the incompressible ideal gas model. Ideal gas equation of state:

$$\rho=\frac{p}{RT_a} \tag{6}$$

where R is the specific gas constant in J/(kg·K).

Heat conduction equation for the solid domain:

$$\nabla\cdot\left(k_s\nabla T\right)=0 \tag{7}$$

where k_s is the thermal conductivity of the solid material in W/(m·K).

Radiative heat transfer is neglected in this study. As shown in Table 2, the thermophysical properties of all materials are listed. The boundary conditions are specified as follows. The initial temperature of the entire model is 293.15 K, i.e., T_∞ = 293.15 K. All six external boundaries of the fluid domain are defined as free pressure boundaries, and the corresponding flow regime is laminar. Initially, the velocity components in the x, y and z directions are all set to zero. The bottom heat source is assigned a constant power of Q = 5 W. Gravity acts in the negative z direction with an acceleration of g = 9.81 m/s^2.

Table 2. Thermophysical properties of materials

Thermophysical properties	Aluminum	Silicon	Air
ρ/kg·m^{-3}	2,719	2,329	Incompressible ideal gas
c_p/J·kg^{-1}·K^{-1}	871	702	1,006.43
k/W·m^{-1}·K^{-1}	202.4	124	0.0242
μ/kg·m^{-1}·s^{-1}	-	-	1.7894e-5

Thermal resistance is taken as the performance evaluation metric, and its calculation formula is given as:

$$R_h = \frac{T_h - T_\infty}{Q} \tag{8}$$

where T_h denotes the temperature of the heat source in K, and Q denotes the power of the heat source in W.

To comprehensively assess the heat dissipation performance and lightweight level of the heat sink under natural convection, this paper introduces the mass-specific heat transfer coefficient h_m, whose calculation formula is expressed as [3]:

$$h_m = \frac{Q}{m(T_h - T_\infty)} \tag{9}$$

The aforementioned governing equations are discretized by the Finite Volume Method (FVM). The second-order upwind scheme is used for the momentum and energy equations, and the PRESTO! scheme is adopted for the pressure term. The coupled algorithm is employed to solve the discretized equations. The residual of the continuity equation is kept below 1×10^{-4}, and the residuals of the energy and momentum equations are kept below 1×10^{-6}.

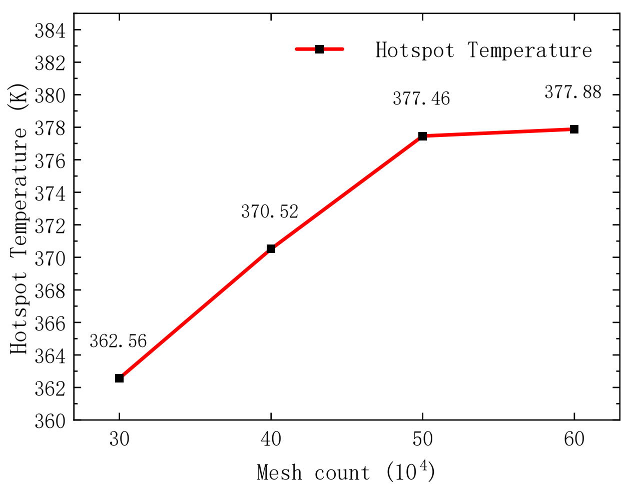

Figure 3. Grid independence verification curve

Figure 3 presents the results of the grid independence verification. When the number of grid cells increases from 506,000 to 603,000, the error in hot-spot temperature is less than 0.2%. The grid with 506,000 cells already meets the simulation requirements, as it can ensure both simulation accuracy and computational efficiency. Accordingly, the grid model with approximately 506,000 cells is finally selected for subsequent calculations.

4. Results and discussion

4.1. Effect of base perforations on heat dissipation performance

This section compares the heat dissipation performance and lightweight metrics of the non-perforated heat sink and the base-perforated heat sink, analyzes the influence patterns of perforations on the natural convection flow field and temperature field, and elucidates the heat dissipation enhancement mechanism based on flow dead zone suppression and chimney effect. Calculated with the heat sink height as the characteristic length, the Rayleigh number of the non-perforated heat sink is R_a = 5×10^5, corresponding to a laminar natural convection flow regime. The perforation scheme with a = 6.5 mm and b = 14.5 mm is defined as the Type I scheme, which is compared with the non-perforated heat sink, and the performance results are presented in Figure 4. The Type I perforated heat sink has a mass of 0.064 kg, 15.79% lower than that of the non-perforated heat sink 0.076 kg. Its thermal resistance drops from 16.86 K/W to 13.92 K/W, with a reduction of 17.44%, and the mass-specific heat transfer coefficient rises from 0.78 W/(kg·K) to 1.12 W/(kg·K), achieving an improvement of 43.59%. Base perforations can significantly reduce thermal resistance while cutting down mass, realizing the synergy of lightweight design and high-efficiency heat dissipation.

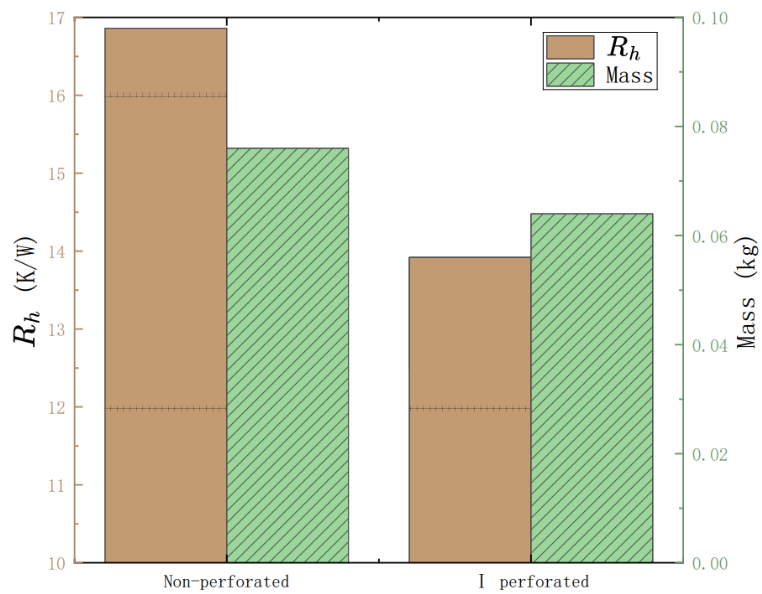

Figure 4. Comparison of thermal resistance and mass between non-perforated heat sink and I perforated heat sink

The improvement of the flow field accounts for the enhanced heat dissipation performance. As shown by the velocity field comparison in Figure 5, for the non-perforated heat sink, airflow can only enter the fin gaps by flowing around from both sides, leading to low airflow velocity at the fin roots and central region, where prominent flow dead zones exist.

After base perforation, through vertical ventilation channels are formed inside the heat sink. Driven by natural convection, these channels generate a chimney effect, drawing air from the lower space into the fin gaps, effectively reducing the flow dead zones at fin roots and reconstructing the overall flow field.

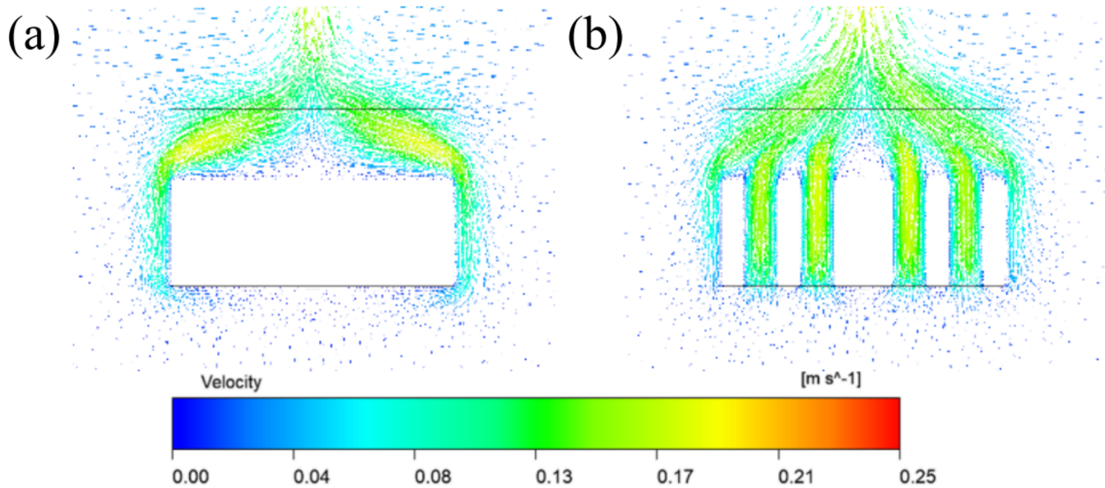

Figure 5. *X–Z* plane comparison of flow velocity vectors. (a) Non-porous heat sink; (b) I perforated heat sink

For both heat sinks, a line probe along the x-direction at y = 4 mm and z = 16 mm is adopted to compare the air velocity within fin gaps, and the results are presented in Figure 6. The black curve corresponds to the air velocity distribution in the fin gaps of the non-perforated heat sink. As observed, the airflow velocity in the central region of the fin gaps decreases rapidly from the side boundaries toward the interior, with an average velocity of only 0.03 m/s, and only the two edge regions maintain relatively high velocities. The velocity profile for the perforated heat sink is marked by the red dashed line. The velocity in the central region is notably elevated, and velocity peaks emerge directly above the perforations; the peak magnitude increases as the position gets closer to the heat sink center. The perforated heat sink yields a higher overall velocity, with an average value of 0.07 m/s, marking a 133% increase compared with the non-perforated heat sink. The most significant velocity improvement occurs in the central region.

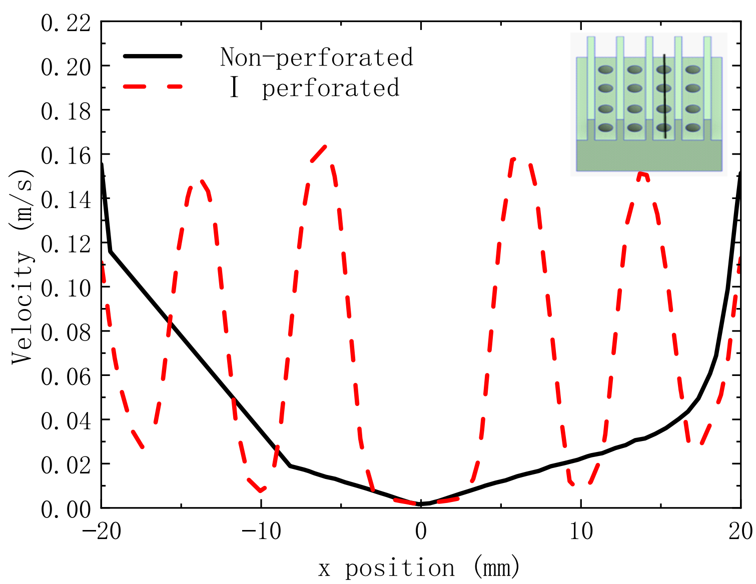

Figure 6. Comparison of velocity in fin gaps

The optimized flow field brings about an improvement in the temperature field. As illustrated by the temperature field comparison in Figure 7, both heat sinks present relatively uniform temperature distribution, which is attributed to the high thermal conductivity of aluminum.

The non-perforated heat sink shows a higher overall temperature level, with its maximum temperature approaching 372 K. After base perforation, the overall temperature of the heat sink decreases remarkably, and heat accumulation is effectively alleviated. The perforations construct through vertical convection channels running through the heat sink; airflow is drawn into the holes from the bottom, forming a temperature gradient inside the channels.

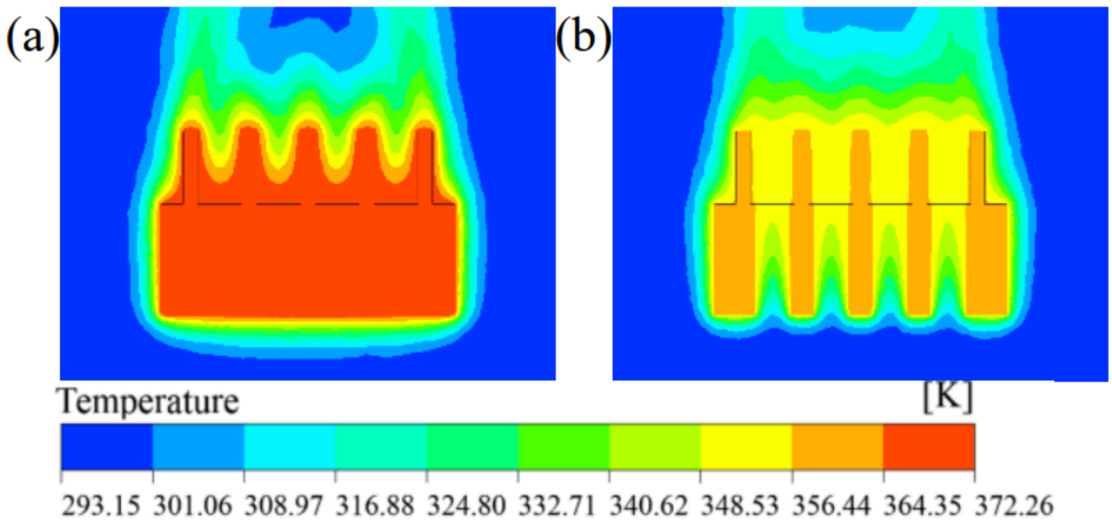

Figure 7. Comparison of temperature distributions on the heat sink. (a) Non-porous heat sink; (b) I perforated heat sink

The above results demonstrate that base perforations can construct vertical convection channels, enhance the chimney effect, reduce flow dead zones at fin roots and increase the average airflow velocity in fin gaps, thereby reducing thermal resistance.

4.2. Effect of perforation shape on heat dissipation performance

As demonstrated in Section 4.1, drilling vertical through holes at the base of finned heat sinks can improve natural convection heat dissipation performance and structural lightweighting by constructing internal ventilation channels within the heat sink. On this basis, the geometric shape of the through holes directly affects the airflow development process, the uniformity of velocity distribution inside the holes and the intensity of the chimney effect, which further influences the overall heat dissipation performance. To clarify the influence mechanism of hole shape on heat dissipation performance, three typical through-hole structures are selected for comparative analysis, namely cylindrical holes, positive frustoconical holes and inverted frustoconical holes. Among them, cylindrical holes are straight-through channels with constant diameter from top to bottom; positive frustoconical holes present a converging frustum shape with a larger lower end and a smaller upper end; inverted frustoconical holes feature a diverging frustum shape with a smaller lower end and a larger upper end.

As shown in Figure 8, the comparison results of thermal resistance under different perforation shapes are presented. To ensure the generality of the research conclusions, comparisons are carried out under multiple sets of typical perforation positions, namely the Type I heat sink with a = 6.5 mm and b = 14.5 mm, the Type II heat sink with a = 4 mm and b = 11 mm, and the Type III heat sink with a = 9 mm and b = 16 mm. The results indicate that under all position conditions, the ranking of thermal resistance from high to low remains consistent: positive frustoconical holes, inverted frustoconical holes, and cylindrical holes.

To reveal the underlying flow mechanism responsible for the difference in heat dissipation performance among different hole shapes, the Type I perforated heat sink is taken as an example to extract and compare the velocity distribution along the central axis of a single hole. The results are presented in Figure 9 and Figure 10. Figure 9(a) shows the velocity distribution inside the cylindrical hole channel. As can be observed from the blue dotted line in Figure 10, after entering the hole, the airflow rapidly develops into steady flow with uniform and smooth velocity distribution, and the average velocity along the central axis reaches 0.17 m/s. The stable and continuous upward airflow facilitates the full play of the chimney effect, continuously drawing cold air from the bottom into the fin gaps and enhancing heat transfer performance.

Figure 9(b) illustrates the velocity distribution inside the positive frustoconical hole channel. As indicated by the black solid line in Figure 10, due to the large inlet cross-section at the lower end, the initial velocity of airflow entering the positive frustoconical hole is relatively low, approximately 0.067 m/s. Although the channel slightly converges along the height direction and exerts a certain acceleration effect on the airflow, with the velocity reaching 0.22 m/s at the hole outlet, the average velocity of the internal airflow along the central axis is as low as 0.15 m/s.

Figure 9(c) depicts the velocity distribution inside the inverted frustoconical hole channel. Combined with the red dashed line in Figure 10, it can be seen that the inverted frustoconical hole has a small inlet cross-section at the lower end, resulting in a relatively high initial airflow velocity of approximately 0.21 m/s. However, as the channel gradually diverges upward, the airflow diffuses rapidly and its velocity decreases to about 0.12 m/s. Despite the high inlet velocity, the overall effective velocity inside the hole is low and the flow stability is poor, so its heat dissipation effect is inferior to that of the cylindrical hole.

Based on the comprehensive comparison of thermal resistance and flow mechanism analysis, it can be concluded that cylindrical holes feature uniform channel geometry, stable flow and remarkable chimney effect, which can most effectively improve the flow condition at fin roots. Therefore, cylindrical holes are the optimal choice among the three hole shapes, followed by inverted frustoconical holes, while positive frustoconical holes perform the worst.

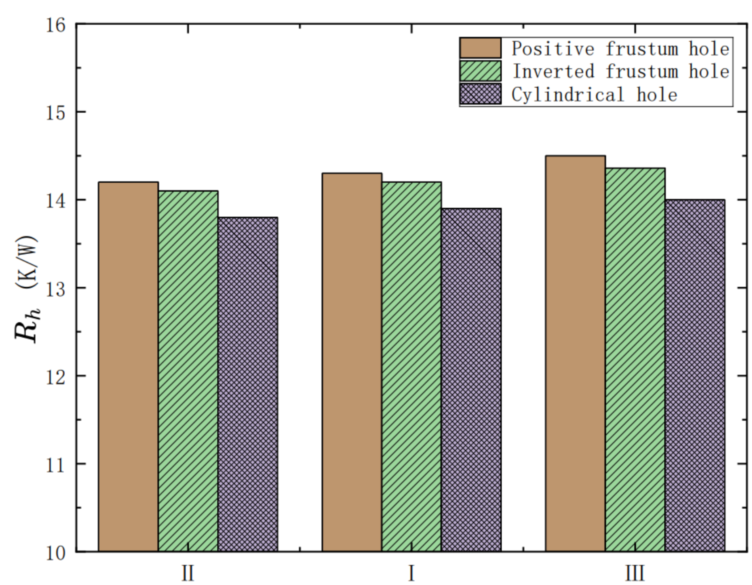

Figure 8. Effect of hole shape on thermal resistance

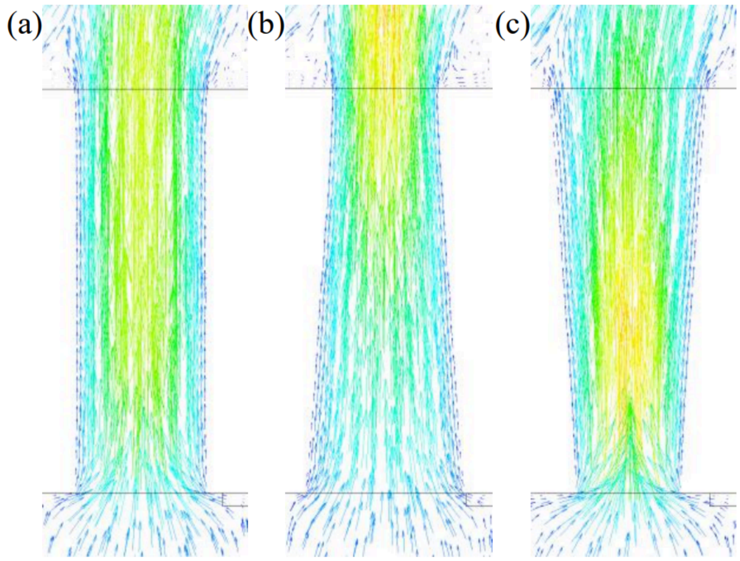

Figure 9. Velocity distribution for different hole shapes. (a) Cylindrical hole; (b) Positive frustum hole; (c) Inverted frustum hole

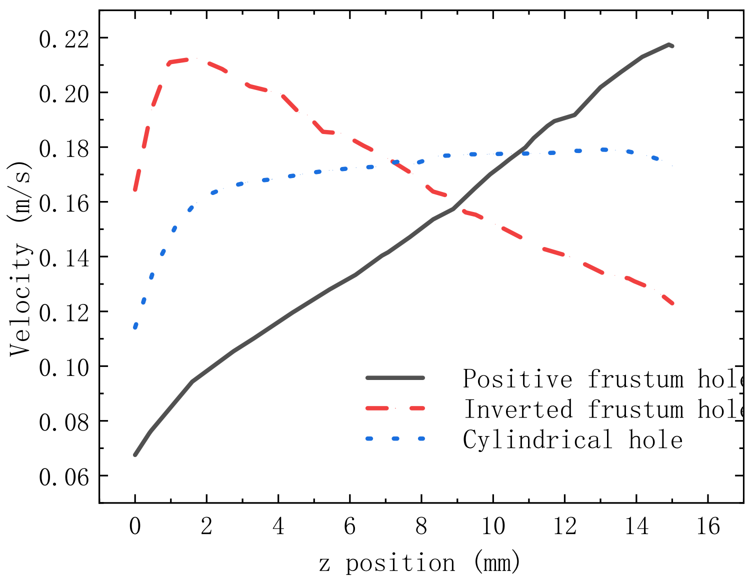

Figure 10. Velocity distribution along the centerline of I perforated heat sink

4.3. Effect of perforation position on heat dissipation performance

On the basis of confirming cylindrical holes as the optimal perforation shape, this section further investigates the influence of the perforation center position on the heat dissipation performance of the heat sink, so as to obtain the optimal perforation layout scheme. With the perforation shape fixed as cylindrical, this section analyzes the influence laws of parameter a (distance from the first row of holes to the Y–Z symmetry plane) and parameter b (distance from the second row of holes to the Y–Z symmetry plane) on thermal resistance, flow field and temperature field.

As shown in Figure 11, the variation pattern of thermal resistance with perforation position is presented. Within the calculation scope of this paper, the thermal resistance of the heat sink shows an overall upward trend with the increase of parameters a and b, indicating that the closer the perforations are to the central area of the heat sink, the better the heat dissipation effect. Comparative analysis reveals that the thermal resistance of the near-heat-source perforation scheme (a = 4 mm, b = 11 mm) is as low as 13.76 K/W, while that of the far-heat-source perforation scheme (a = 9 mm, b = 16 mm) is relatively higher. By comparison, the near-heat-source scheme can further reduce the thermal resistance by 2.06%.

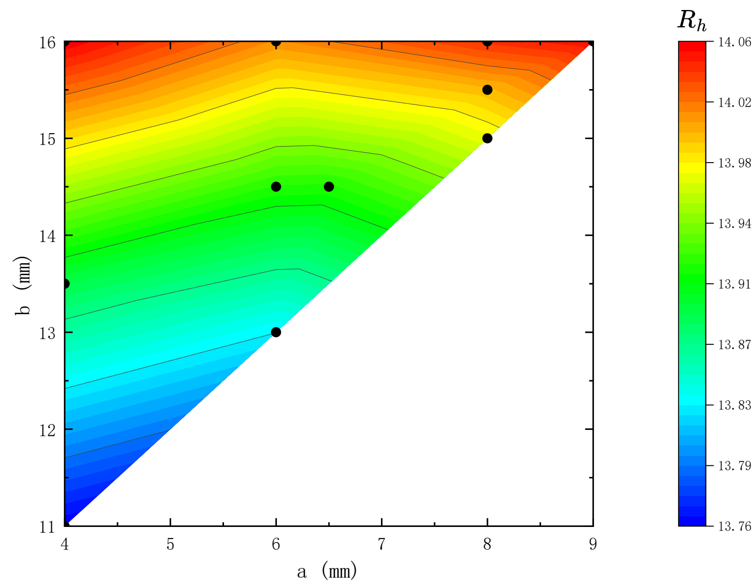

Figure 11. Variation of R_h with perforation location parameters a and b

To reveal the underlying flow mechanism by which perforation position influences heat dissipation, the two typical schemes mentioned above are selected for flow field comparison, and the results are presented in Figure 12.

Both schemes can generate vertical upward chimney airflow via the base through holes, enabling cold air to pass through the base and flow into the fin gaps. However, for the far-heat-source scheme, as the perforations deviate from the central region, the channels fail to effectively cover the core area of the fin roots, leaving prominent flow dead zones at the fin roots.

In comparison, the through holes in the near-center scheme are arranged closer to the heat source, which can directly build high-efficiency vertical ventilation channels in the high heat flux region, remarkably narrowing the range of dead zones and improving the overall airflow utilization efficiency.

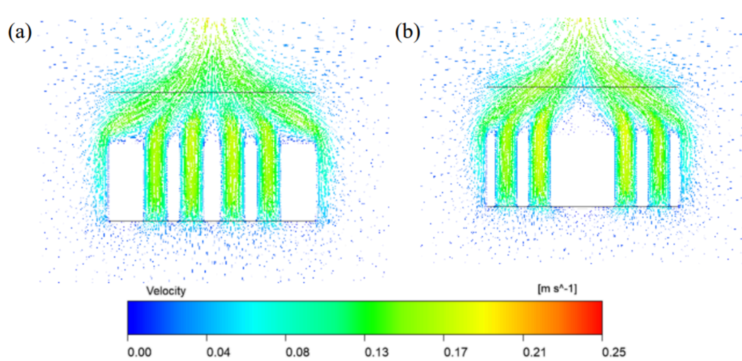

Figure 12. Comparison of flow velocity vectors on X–Z plane. (a) Heat sink with near-heat-source perforation; (b) Heat sink with far-heat-source perforation

As shown in Figure 13, the temperature field distributions under different perforation positions are presented. For the near-center scheme, the high-temperature region is effectively confined to a small area directly above the heat source, with a lower overall temperature level and smoother heat diffusion and dissipation. In contrast, the far-center scheme suffers from insufficient heat transfer in the central region due to the offset perforation positions; heat cannot be removed in a timely manner, leading to a higher overall temperature level.

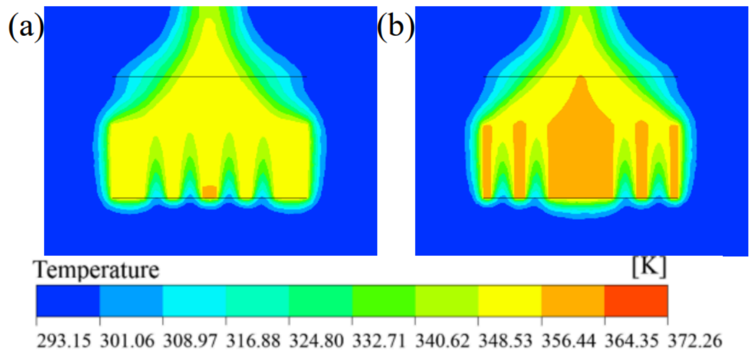

Figure 13. Comparison of temperature distributions on the heat sink. (a) Heat sink with near-heat-source perforation; (b) Heat sink with far-heat-source perforation

The above results demonstrate that the perforation position directly determines the coverage capacity of vertical channels over the core heat-generating area. Placing cylindrical holes close to the heat source can more fully strengthen the chimney effect and suppress flow dead zones, thereby achieving superior heat dissipation performance.

5. Conclusion

Base perforation on finned heat sinks can effectively reconstruct the natural convection flow field, open up vertical ventilation channels at the bottom, reduce flow dead zones at fin roots, increase the airflow velocity in fin gaps, optimize the temperature field distribution and lower the overall temperature level of the heat sink. In this model, the perforation scheme with a = 6.5 mm and b = 14.5 mm reduces the thermal resistance by 17.44% and increases the mass-specific heat transfer coefficient by 43.59% compared with the non-perforated scheme.

Perforation shape has a significant impact on heat dissipation performance. Cylindrical through holes feature stable internal airflow velocity and a more prominent chimney effect, delivering the optimal heat transfer enhancement effect, followed by inverted frustoconical holes, while positive frustoconical holes perform the worst.

Perforation position exerts a remarkable influence on the heat dissipation performance of the heat sink. The thermal resistance shows an upward trend as the distance between the perforation position and the heat sink center increases. When perforations are arranged in the area close to the heat source, the internal airflow organization is more reasonable and the heat dissipation effect reaches the optimum. In this model, the optimal position corresponds to a = 4 mm and b = 11 mm, with a thermal resistance of 13.76 K/W, which is 2.06% lower than that of the worst position with a = 9 mm and b = 16 mm.

References

[1] Abo-Zahhad, E. M., Ookawara, S., Radwan, A., Elkady, M. F., & El-Shazly, A. H. (2020). Optimization of stepwise varying width microchannel heat sink for high heat flux applications. *Case Studies in Thermal Engineering, 18*, 100587. https://doi.org/10.1016/j.csite.2020.100587

[2] Abbas, A., & Wang, C.-C. (2020). Augmentation of natural convection heat sink via using displacement design. *International Journal of Heat and Mass Transfer, 154*, 119757. https://doi.org/10.1016/j.ijheatmasstransfer.2020.119757

[3] El Ghandouri, I., El Maakoul, A., Saadeddine, S., & Meziane, M. (2020). Design and numerical investigations of natural convection heat transfer of a new rippling fin shape. *Applied Thermal Engineering, 178*, 115670. https://doi.org/10.1016/j.applthermaleng.2020.115670

[4] Altun, A. H., & Ziylan, O. (2019). Experimental investigation of the effects of horizontally oriented vertical sinusoidal wavy fins on heat transfer performance in case of natural convection. *International Journal of Heat and Mass Transfer, 139*, 425–431. https://doi.org/10.1016/j.ijheatmasstransfer.2019.05.009

[5] Chu, W. X., Tsai, M. K., Jan, S. Y., Huang, H. H., & Wang, C.-C. (2020). CFD analysis and experimental verification on a new type of air-cooled heat sink for reducing maximum junction temperature. *International Journal of Heat and Mass Transfer, 148*, 119094. https://doi.org/10.1016/j.ijheatmasstransfer.2019.119094

[6] Hussain, A. A., Freegah, B., Khalaf, B. S., & Towsyfyan, H. (2019). Numerical investigation of heat transfer enhancement in plate-fin heat sinks: Effect of flow direction and fillet profile. *Case Studies in Thermal Engineering, 13*, 100388. https://doi.org/10.1016/j.csite.2018.100388

[7] Nilpueng, K., Mesgarpour, M., Asirvatham, L. G., Dalkılıç, A. S., Ahn, H. S., Mahian, O., & Wongwises, S. (2021). Effect of pin fin configuration on thermal performance of plate pin fin heat sinks. *Case Studies in Thermal Engineering, 27*, 101269. https://doi.org/10.1016/j.csite.2021.101269

[8] Moayedi, H., & Ghannad Bajestani, A. (2025). Improvement of heat sink cooling performance by optimizing geometrical parameters: Role of fin number, height, and angle. *International Communications in Heat and Mass Transfer, 169*, 109859. https://doi.org/10.1016/j.icheatmasstransfer.2025.109859

[9] Zhang, K., Li, M.-J., Wang, F.-L., & He, Y.-L. (2020). Experimental and numerical investigation of natural convection heat transfer of W-type fin arrays. *International Journal of Heat and Mass Transfer, 152*, 119315. https://doi.org/10.1016/j.ijheatmasstransfer.2020.119315

[10] Karlapalem, V., & Dash, S. K. (2021). Design of perforated branching fins in laminar natural convection. *International Communications in Heat and Mass Transfer, 120*, 105071. https://doi.org/10.1016/j.icheatmasstransfer.2020.105071

[11] Sultan, H. S., Saleem, K. B., Alshammari, B. M., Turki, M., Aydi, A., & Kolsi, L. (2024). Numerical investigation of natural convection from a horizontal heat sink with an array of rectangular fins. *Case Studies in Thermal Engineering, 61*, 104877. https://doi.org/10.1016/j.csite.2024.104877

[12] Awasarmol, U. V., & Pise, A. T. (2015). An experimental investigation of natural convection heat transfer enhancement from perforated rectangular fins array at different inclinations. *Experimental Thermal and Fluid Science, 68*, 145–154. https://doi.org/10.1016/j.expthermflusci.2015.04.008

[13] Li, J., Jasim, D. J., Kadir, D. H., Maleki, H., Esfahani, N. N., Shamsborhan, M., & Toghraie, D. (2024). Multi-objective optimization of a laterally perforated-finned heat sink with computational fluid dynamics method and statistical modeling using response surface methodology. *Engineering Applications of Artificial Intelligence, 130*, 107674. https://doi.org/10.1016/j.engappai.2023.107674

[14] Awasarmol, U. V., Pise, A. T., Patil, J. D., Jathar, L. D., & Verma, R. R. (2023). Experimental investigation of heat transfer enhancement by using perforated fin array having different perforation ratios, angle of inclination and configuration of fins under forced convection condition. *International Communications in Heat and Mass Transfer, 147*, 106995. https://doi.org/10.1016/j.icheatmasstransfer.2023.106995